Method for auto-alignment and determination of parameter space in dual-phase grating interferometry

RUIZHI TANG,[1,2,*] **WANNES GOETHALS,**[1,2]
CAORI ORGANISTA,[1,2,3,4] **LUC VAN HOOREBEKE,**[1,2]
MARCO STAMPANONI,[3,4] **JAN AELTERMAN,**[1,2,5]
AND MATTHIEU N. BOONE[1,2]

[1]*Ghent University Centre for X-Ray Tomography (UGCT), Proeftuinstraat 86/N12, 9000 Ghent, Belgium*
[2]*Radiation Physics research group, Department of Physics and Astronomy, Ghent University, Proeftuinstraat 86, 9000 Ghent, Belgium*
[3]*Swiss Light Source, Paul Scherrer Institute, 5232 Villigen, Switzerland*
[4]*Institute for Biomedical Engineering, ETH Zurich, 8092 Zurich, Switzerland*
[5]*IPI-TELIN-IMEC, Ghent University, Ghent, Belgium*
*Ruizhi.Tang@UGent.be

Abstract: X-ray dual-phase grating interferometry provides quantitative micro-structural information beyond the optical resolution through its tunable correlation length. Ensuring optimal performance of the set-up requires accurate correlation length estimation and precise alignment of the gratings. This paper presents an automated procedure for determining the complete geometrical parameters of the interferometer set-up with a high degree of precision. The algorithm's effectiveness is then evaluated through a series of experimental tests, illustrating its accuracy and robustness.

1. Introduction

X-ray Talbot(-Lau) grating interferometry (XT-GI) has attracted a lot of research interest over the past decades and has proven its huge potential in medical imaging and material science [1–10]. XT-GI demonstrates the capability to simultaneously provide three complementary signals: conventional absorption, differential phase contrast, and dark-field signal. In contrast to traditional X-ray radiography, which primarily relies on absorption contrast, the phase signal is highly sensitive to electron density fluctuations, providing superior contrast for low-Z materials, while the dark-field signal provides access to unresolvable micro-structural information. The principle of this technique is based on the Talbot effect [11], in which a phase grating is used to split the incident beam and produce the reference patterns at the fractional Talbot distances, and an absorption grating is used to resolve the generated patterns. By quantitatively analyzing how the reference pattern is distorted by a sample, the three complementary signals can subsequently be retrieved.

However, the absorption grating behind the sample blocks almost half of the information-carrying photons, significantly reducing the dose efficiency. To resolve this challenge, Miao et al. and Kagias et al. proposed the dual-phase grating interferometry (DPGI) [12,13]. A schematic of a generic implementation of the DPGI is depicted in Fig. 1. Two identical phase gratings, G_1 and G_2, are placed between the X-ray source and the detector, with $R_g \ll R_1 \approx R_2$. Due to the cone beam geometry, the slight difference in the magnification factors between the two gratings generates resolvable Moiré fringes whose period is much larger than the pitch sizes of the gratings, and the derivations of the fringe formation mechanism will be illustrated in section 2. Therefore, the absorption grating is not required in DPGI. Another main advantage

DPGI provides is that the correlation length can be easily adjusted by the inter-grating distance R_g, thereby not influencing the sample's magnification. The correlation length is a parameter to characterize the beam separation [14], which is proportional to the spatial locations of two gratings, given as [15]:

$$\xi \propto \frac{R_g}{R_1 + R_2}. \tag{1}$$

Since the relation between the correlation length and the dark-field signal reveals the quantitative small-angle scattering (SAS) information [16,17], the configuration of DPGI is promising to implement this technique.
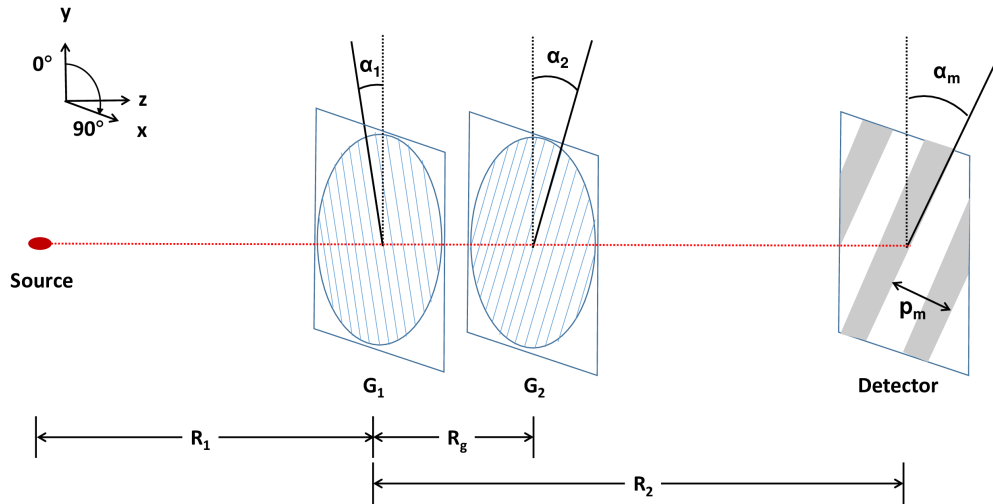

Fig. 1. Schematic of dual-phase grating interferometry. X-rays are generated by the x-ray tube, propagate through the two gratings, and are subsequently captured by the detector. R_1, R_2, R_g represent source-to-G_1, G_1-to-detector, and inter-grating distances, respectively. Moreover, the rotated angles for two gratings are denoted as α_1 and α_2. The generated Moiré pattern can be directly resolved by the detector, and the angle and period of the fringe are represented as α_m and p_m, respectively.

To obtain reliable results, two challenges need to be resolved. Firstly, to precisely estimate the correlation length, the distances R_1, R_2, and R_g, as shown in Fig. 1, should be measured with high accuracy. Especially, since the inter-grating distance R_g is normally small between 1 and 10 mm, the desired measurement error for it should be within tens of micrometers to avoid noticeable deviations when estimating the correlation length. However, achieving such precision is challenging or even impossible when employing a conventional ruler-based approach for distance measurement. This difficulty is aggravated by the fixed placement of the gratings within metallic frames, rendering the accurate positions unobservable from view. Secondly, the gratings need to be aligned to ensure optimal performance. This means that the lamellas of the two gratings remain parallel and are oriented vertically with respect to the stepping direction (x-axis), with $\alpha_1 = \alpha_2 = 0$ (see Fig. 1). One intuitive way for aligning the two gratings involves the rotation of one grating until the Moiré pattern appears upright ($\alpha_m \approx 0$). However, the angle of the other grating remains undetermined, rendering the angle of the Moiré pattern unsuitable as an indicator of alignment. Furthermore, the orientation determination of the pattern rests upon human assessment, introducing subjectivity and potential inaccuracies. Moreover, aligning under supervision is a laborious and time-consuming task.

In this work, based on the properties of the Moiré patterns, we develop an automated workflow encompassing image acquisition and subsequent data analysis, to ensure the precise determination

of all relevant geometrical parameters: three distances (R_1, R_2, R_g) and two angles (α_1, α_2). Furthermore, the accuracy and robustness of the algorithm are validated by the experimental results.

2. Method

2.1. Moiré patterns formation mechanism in DPGI

The Moiré patterns in DPGI are formed by a cross-modulation between the individual patterns generated by the two gratings [18,19]. First, we consider the situation when two identical gratings are aligned. The intensity pattern generated solely by G_1 is represented by $\exp\left(\frac{i2\pi lx}{M_1 p_g}\right)$, where l indexes the diffraction order and p_g is the pitch size of the grating. The magnification factor for G_1 is given as: $M_1 = \frac{R_1+R_2}{R_1}$. Similarly, in the absence of G_1, the intensity pattern for a diffraction order generated by G_2 is represented by $\exp\left(\frac{i2\pi rx}{M_2 p_g}\right)$, with r the diffraction order and the magnification factor $M_2 = \frac{R_1+R_2}{R_1+R_g}$. Then, the relative intensity oscillation of the cross-modulation can be represented as [19]:

$$I_c(x) = \exp\left[i2\pi\left(\frac{l}{M_1 p_g} + \frac{r}{M_2 p_g}\right)x\right]. \tag{2}$$

Only when $r = -l$, the resultant Moiré patterns, characterized by sufficiently low frequencies, can be directly resolved. Meanwhile, other fringes that cannot be resolved merely add to the background signal. Consequently, the relative intensity oscillation of the Moiré pattern corresponding to the diffraction order l is expressed as follows [19]:

$$I_m(x) = \exp\left[\frac{-i2\pi l}{p_g}\left(\frac{R_g}{R_1 + R_2}\right)x\right]. \tag{3}$$

The recorded interference pattern consists of a fundamental frequency and its harmonics.

2.2. Geometrical relationships between Moiré fringe and gratings

According to Eqs. (2) and (3), the Moiré patterns in DPGI originate from the basic patterns formed by individual gratings. Moreover, based on the derivations given by Gabrielyan et al. [20], the angle and period of the Moiré pattern are formulated as functions of the corresponding angles and periods of two basic patterns. Therefore, the angle α_m of the Moiré pattern formed in DPGI (see Fig. 1) can be expressed as:

$$\alpha_m(\alpha_1, \alpha_2, R_g, R_1) = \arcsin\frac{(R_1 + R_g)\sin\alpha_2 - R_1\sin\alpha_1}{\sqrt{(R_1 + R_g)^2 + R_1^2 - 2R_1(R_1 + R_g)\cos(\alpha_2 - \alpha_1)}}, \tag{4}$$

where α_1 and α_2 represent the rotated angles of the gratings, as indicated in Fig. 1. Furthermore, the period p_m of the Moiré pattern for the first diffraction order ($l = 1$) is given as:

$$p_m(\alpha_1, \alpha_2, R_g, R_1, R_2, p_g) = \frac{(R_1 + R_2)p_g}{\sqrt{(R_1 + R_g)^2 + R_1^2 - 2R_1(R_1 + R_g)\cos(\alpha_2 - \alpha_1)}}. \tag{5}$$

The derivations for Eqs. (4) and (5) are illustrated in Appendix.

2.3. Geometrical parameters determination

The principle of the algorithm for determining the geometrical parameters is based on the relationships as provided by Eqs. (4) and (5), elucidating how the Moiré patterns change with the

geometrical configurations. Within the context of our experimental set-up, the adjustment of the geometrical configuration is achieved through the rotation of the two gratings in the xy-plane and the controlled movement of G_2 along the z-axis to fine-tune the inter-grating distance. The angular deviations are denoted as $\Delta\alpha_1$ and $\Delta\alpha_2$, representing the relative rotated angles of the two gratings. Additionally, the relative displacement of G_2 is represented by the parameter Δd. All these relative movements are precisely controlled by the motors.

To determine the initial geometrical parameters (α_1, α_2, R_g, R_1, R_2), a series of adjustments are made to the geometrical configuration. For each configuration indexed as n, one Moiré pattern is recorded, and the corresponding angle $\hat{\alpha}_m^n$ and period for the first diffraction order $\hat{p}_m^n$ are extracted from the images. The quantities denoted by hats represent the results obtained from measurements. Utilizing Eqs. (4) and (5), the expected angle and period for each configuration are mathematically modelled as $\alpha_m^n(\alpha_1+\Delta\alpha_1^n, \alpha_2+\Delta\alpha_2^n, R_g+\Delta d^n, R_1)$ and $p_m^n(\alpha_1+\Delta\alpha_1^n, \alpha_2+\Delta\alpha_2^n, R_g+\Delta d^n, R_1, R_2, p_g)$, respectively. Firstly, four initial geometrical parameters (α_1, α_2, R_g, R_1) are retrieved by minimizing the sum of squares of the difference between the measured and expected Moiré angle, formulated as:

$$(\alpha_1, \alpha_2, R_g, R_1) = \arg\min \sum_{n=1}^{N} \left[\hat{\alpha}_m^n - \alpha_m^n(\alpha_1 + \Delta\alpha_1^n, \alpha_2 + \Delta\alpha_2^n, R_g + \Delta d^n, R_1)\right]^2. \qquad (6)$$

Subsequently, combining the extracted parameters from Eq. (6) and the knowledge of the grating pitch size p_g, the determination of R_2 is realised by minimizing the summation of the squared residuals of Moiré periods for the first diffraction order. The optimization process is formulated as:

$$R_2 = \arg\min \sum_{n=1}^{N} \left[\hat{p}_m^n - p_m^n(\alpha_1 + \Delta\alpha_1^n, \alpha_2 + \Delta\alpha_2^n, R_g + \Delta d^n, R_1, R_2, p_g)\right]^2. \qquad (7)$$

2.4. Extraction of angle and period information from Moiré fringes

To implement the optimization processes outlined in Eqs. (6) and (7), an image processing algorithm is developed to automatically extract the angle $\hat{\alpha}_m^n$ and the period $\hat{p}_m^n$ from the recorded
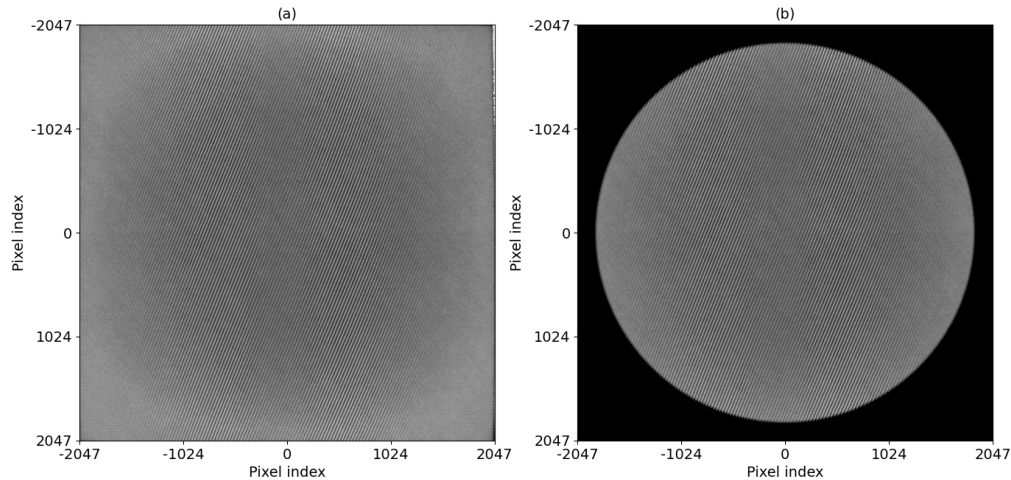

Fig. 2. A normalized image is shown in (a), where evident artefacts resulting from geometric distortion are observable at the image's boundaries. To mitigate the influences of the geometrical distortion and prepare for a two-dimensional Fourier transform, the normalized image is masked by a circular window, as shown in (b).
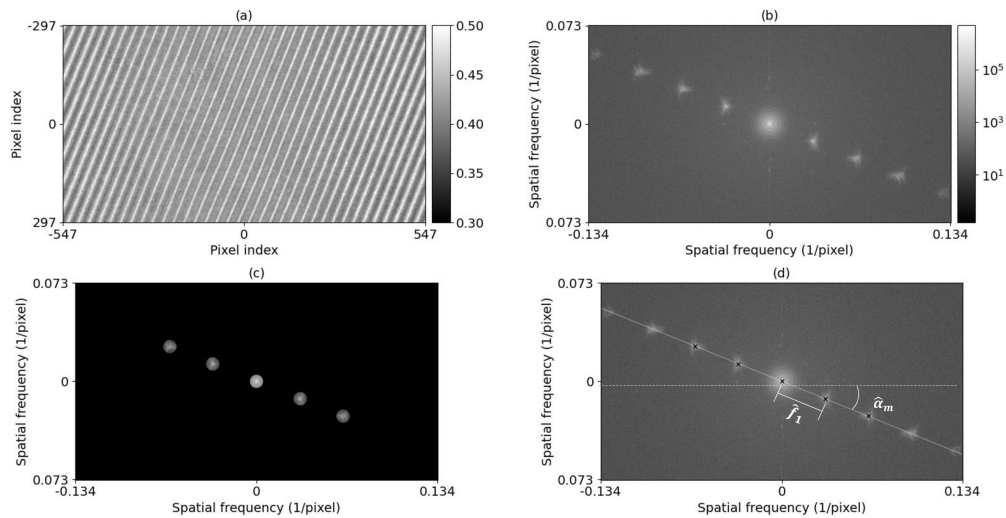
Fig. 3. The process to extract angle and period from Moiré fringe. The images in real and Fourier space are depicted in (a) and (b), respectively. To facilitate visualization, only the central regions of interest are displayed for both images. Based on the magnitudes in Fourier space, several peaking positions are identified and small circular regions are segmented around these peaking positions, as shown in (c). The center of mass for each isolated region is calculated and marked as the black cross in (d). A line is fitted to the location information, and the angle spanned between the fitted line and the horizontal axis provides the angle of the Moiré fringe, denoted as $\hat{\alpha}_\mathrm{m}$. Moreover, the distance between the first harmonics and the fundamental frequency is represented as $\hat{f}_1$, which indicates the frequency of the pattern.

Moiré patterns. Firstly, to remove the fixed-pattern noise, which originates from the dark current and variations in pixel sensitivity, the captured image is normalized based on a dark image and a flat-field image. Presented in Fig. 2(a) is a representative instance of a normalized image. Subsequently, a circular window is applied to the normalized image (see Fig. 2(b)), whereby the amplitude remains consistent within the kernel while diminishing exponentially to zero at the periphery. There are two reasons to perform this windowing process. Firstly, to prepare for a two-dimensional Fourier transform, the sharp transition changes at the boundary should be removed to diminish the effect of spectral leakage. Secondly, it can be seen from Fig. 2(a) that the image is subject to geometric distortions introduced by the presence of fiber optics integrated within the detector. Especially, these distortions are particularly pronounced at the image's peripheries. Therefore, the windowing process serves to mitigate the impact of both of these effects.

Then, the windowed image is transformed into the Fourier space. For better visualization, the zoomed images corresponding to the real and Fourier spaces are displayed in Fig. 3(a) and (b), respectively. Logarithmic magnitudes are employed to visualize the image in Fourier space. Given that the harmonics within the Fourier space respond sensitively to both the orientation and frequencies of the periodic patterns, the Fourier domain provides accurate information for extracting the angle and period of the Moiré pattern. Based on the Fourier space magnitudes, distinct peaking positions can be located. At each of these peaking positions, a small circular region is isolated, as depicted in Fig. 3(c). The center of mass within each segmented region is subsequently calculated, representing its spatial frequency and orientation. As shown in Fig. 3(d), the located positions are denoted by black crosses. These positions are subjected to a linear fitting process, and the fitted line is plotted as the white solid line. The angle of Moiré pattern $\hat{\alpha}_\mathrm{m}$ is determined by the angle spanned between the fitted line and the horizontal axis. Moreover, the

frequency for the harmonic k is related to the Fourier distance between the harmonic's position and the origin, denoted as $\hat{f}_k$. The Fourier space is discretized with intervals of $\frac{1}{N_d}$, where the unit is periods per pixel. Considering that the detector dimensions are equal in both the x and y axis, the number of pixels for each dimension is represented as N_d. According to the located positions for all harmonics, the period of the Moiré pattern for the first diffraction order can be estimated as:

$$\hat{p}_m = p_d \cdot \frac{\sum_{k=1}^{K} \frac{k}{\hat{f}_k}}{K}, \tag{8}$$

where p_d represents the pixel size. Since the negative harmonics contain the same information as positive ones, it is adequate to use only positive harmonics ($k > 0$) to determine the first-diffraction-order period. To ensure accurate results empirically, a minimum of five identified positions ($K \geq 2$) is required for the retrieval of angles and periods. Moreover, the average distance of identified positions (black crosses in Fig. 3(d)) from the fitted line should be lower than $\frac{1}{N_d}$. Failure to satisfy these two criteria results in the exclusion of the corresponding Moiré pattern from subsequent optimization procedures.

3. Experiment and results

3.1. Experimental settings

X-rays were generated by a transmission-type microfocus X-ray tube (FXT-160.51, FEINFOCUS GmbH, Germany), employing a 1 µ tungsten-coated CVD diamond anode. The tube operated in microfocus mode at 40 kV tube voltage and 200 µA filament current. Recordings of images were carried out using an sCMOS camera (Gsense, PHOTONIC SCIENCE, UK) with a 100 µ CsI:TI scintillator. The detector featured an active input area of 67×67 mm^2 and an effective pixel size of 16.4×16.4 µ^2, resulting in a total of 4095×4095 pixels. Two identical phase gratings were etched into silicon substrates of 250 µ thickness, reaching the same depth of 28 µ, as detailed in a previous publication [21]. The depth of 28 µ induced a π phase-shift at the photon energy of 22 keV. The grating pattern was realized with a period of 1 µ and a duty cycle of 0.5. The set-up's total distance spanning from the source to the detector was maintained at approximately 1 m, with G$_1$ positioned approximately at the midpoint between the source and the detector. G$_2$ was located downstream and in close proximity to G$_1$. Four motors were utilized to precisely control the movements of the two gratings. Two goniometer stages (CGO-77.5, SmarAct GmbH, Germany) were employed to independently rotate the two gratings within the xy-plane. These stages offer a travel range of $+/-5$ degrees and a resolution of approximately 7 micro-degrees. To adjust the inter-grating distance, a linear stage (CLS-5282-L, SmarAct GmbH, Germany) was used to move G$_2$ along the z-axis. This stage declares a travel range of 51 mm and a resolution of 4 nm. Another linear stage (CLS-5252-L, SmarAct GmbH, Germany) was utilized to move G$_1$ along the x-axis, enabling the phase stepping technique [3,13]. This stage has a declared travel range of 31 mm and 4 nm resolution.

To adjust the geometrical configuration, the following steps are taken. Firstly, with G$_2$ kept static at the initial angle α_2, G$_1$ is rotated from $\alpha_1 - 0.4$ to $\alpha_1 + 0.4$ degrees with a step size of 0.08 degree, resulting in a total of 11 discrete steps. Then, with G$_1$ held at its initial angle α_1, the rotation for G$_2$ is executed from $\alpha_2 - 0.4$ to $\alpha_2 + 0.4$ degrees. Following this, the inter-grating distance is adjusted through the displacement of G$_2$. The rotation process for the two gratings is then repeated for each inter-grating distance. The displacement of G$_2$ from its initial position R_g spans from 0 to 5 mm, with a step size of 0.5 mm. Figure 4(c) exemplifies the adjustment of the geometrical configuration. In total, 242 distinct geometrical configurations are achieved, and for each configuration, the Moiré pattern is recorded with an exposure time of 15 s. The whole image acquisition process is fully automated.
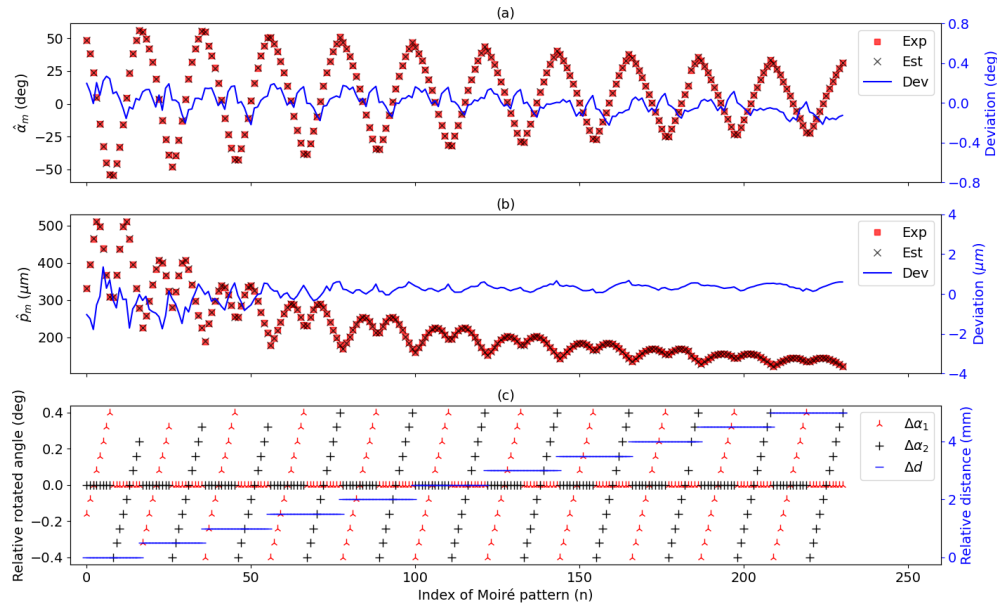
Fig. 4. Illustration of the deviations between the experimental and estimated results among the used Moiré patterns. (a) compares the extracted Moiré angles (red squares) and estimated ones (black crosses) for each Moiré pattern. The deviations between the experimental and estimated results are represented as a blue line, and the corresponding values are displayed on the secondary y-axis on the right-hand side. Similarly, (b) illustrates the results for the Moiré periods. The average absolute deviations between the experimental and estimated results are $0.0811°$ for the angles and 0.3757μ for the periods, which is quite accurate compared to the range of $-60°$ to $60°$ degrees and 100 to 500μ. (c) presents the corresponding geometrical configuration for each Moiré pattern. The relative rotated angles of G_1 and G_2 are represented as red upward-pointing triangles and black pluses, respectively. The relative displacements of G_2 from the initial inter-grating distance are represented as blue horizontal lines and the corresponding values are displayed on the secondary y-axis on the right-hand side.

3.2. Results

To determine the geometrical parameters, all 242 Moiré patterns are analyzed by the proposed algorithm to extract the corresponding angles and periods, as elaborated in section 2.4. As previously mentioned, certain Moiré patterns are excluded if they fail to meet the two criteria established to ensure accuracy. The extracted angles and periods are shown in Fig. 4(a) and (b), respectively, represented as red squares. The current dataset consists of 231 Moiré patterns that are used for the following optimization process. Based on Eqs. (6) and (7), the initial geometrical parameters are extracted, yielding: $R_1 = 0.5024$ m, $R_2 = 0.5018$ m, $R_g = 1.9539$ mm, $\alpha_1 = -1.2794°$ and $\alpha_2 = -1.1762°$. In Fig. 4(a) and (b), the black cross represents quantities estimated by the model for different geometrical configurations (refer to Eqs. (4) and (5)), utilizing the extracted initial geometrical parameters. The corresponding deviations between the experimental and estimated results are shown as blue lines in Fig. 4(a) and (b). The notably low deviations between the experimental and estimated values imply the accurate determination of the initial parameters. The average absolute deviations for angles and periods are $0.0811°$ and 0.3757μ, respectively. Figure 4(c) illustrates the corresponding geometrical configuration ($\Delta\alpha_1$, $\Delta\alpha_2$ and Δd) for each Moiré pattern.

If the initial values read from the two goniometers are represented as A'_1 and A'_2, then the aligned positions for the goniometers are calculated as $A_1 = A'_1 - \alpha_1$ and $A_2 = A'_2 - \alpha_2$, respectively. Figure 5(a) and (b) illustrate the recorded Moiré patterns before and after the alignment, respectively. According to Eq. (4), when two gratings are aligned the Moiré pattern should be vertical ($\hat{\alpha}_m = 0$), a characteristic that can be visually confirmed in Fig. 5(b). Moreover, the average visibility $\overline{V}$ is compared between Fig. 5(a) and (b) within the depicted field of view, which illustrates the fringe contrasts in the transverse axis (x-axis). The visibility for the pixel (i, j) is determined by searching for the minimum and maximum intensity values within the pixel range from (i, j) to $(i + p_t, j)$, denoted as $I_{\min}(i, j)$ and $I_{\max}(i, j)$. p_t represents the period of the fringe along the transverse axis, specified in pixels. Then the visibility is calculated as:

$$V(i,j) = \frac{I_{\max}(i,j) - I_{\min}(i,j)}{I_{\max}(i,j) + I_{\min}(i,j)}, \tag{9}$$

Compared between Fig. 5(a) and (b), the average visibility experiences a 5% increase after the alignment process. Additional discussions about the relationship between misalignment and visibility are given in section 4.
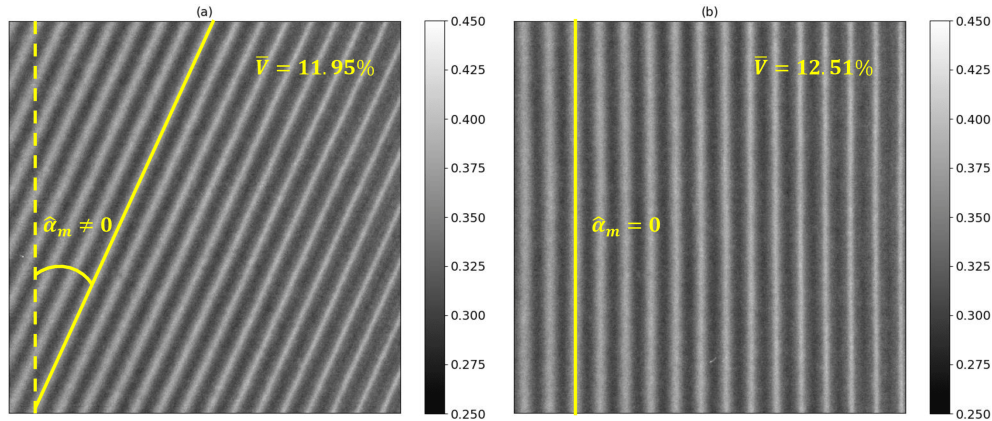

Fig. 5. The interference patterns are depicted before (a) and after (b) the alignment process, with the inter-grating distance at the initial value $R_g = 1.9539$ mm. The average visibility within the depicted field of view is increased from 11.95% to 12.51% after the alignment process.

The geometrical determination procedure is independently repeated five times, with different initial angles of two gratings. Therefore, by comparing the extracted geometrical parameters across these procedures, the algorithm's accuracy and robustness are evaluated. Moreover, instead of using the complete dataset from each procedure, the number of Moiré patterns used for fitting is gradually increased from 5 to 220 to evaluate the relationship between the size of the dataset and the accuracy of the algorithm. In order to diminish the potential correlations among the geometrical configurations, the Moiré patterns used for fitting are randomly picked from the full dataset. Then, for each dataset size, the initial geometrical parameters are retrieved, and the corresponding mean value and standard deviation are calculated among the five independent procedures. The statistical results for the parameters related to the three distances are shown in Fig. 6(a) - (c). The mean values are depicted as black lines, while the grey background illustrates the standard deviations. Figure 6(d) and (e) illustrate the results for the aligned positions of two goniometers. Moreover, Fig. 6(f) presents the results of the differences in readout values between the two goniometers, which provide insights into the accuracy and robustness of achieving the same orientations for the two gratings. Overall, with the dataset size increased, the retrieval
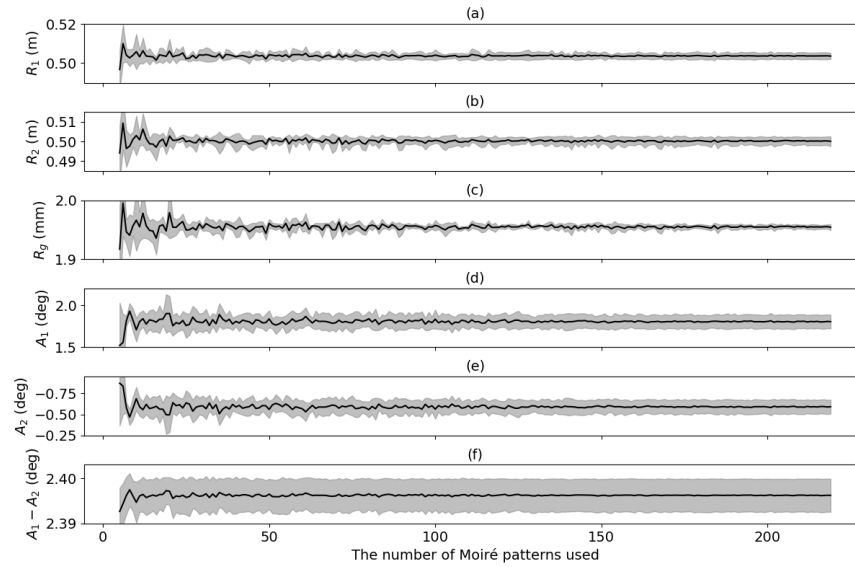
Fig. 6. The accuracy and robustness of the algorithm are evaluated by examining the relationships between the extracted geometrical parameters among five independent procedures and the number of Moiré patterns used for fitting. The number of Moiré patterns used varies from 5 to 220. For each size of the dataset, the mean and standard deviation are calculated from five procedures. As the dataset size increases, the retrieval of all parameters, namely R_1, R_2, R_g, A_1, A_2, and $A_1 - A_2$, becomes more consistent and stable.

Table 1. Mean values and standard deviations of the six parameters that the algorithm can retrieve when the dataset size is 220.

Parameter	Unit	Mean value	Standard deviation
R_1	m	0.5036	0.0015
R_2	m	0.5001	0.0025
R_g	mm	1.9541	0.0050
A_1	degree	1.8047	0.0815
	rad	0.0315	0.0014
A_2	degree	−0.5916	0.0835
	rad	−0.0103	0.0015
$A_1 - A_2$	degree	2.3962	0.0037
	rad	0.0418	0.0001

of all six geometrical quantities becomes more accurate, indicated by more stable mean values and lower standard deviations. This is expected, as the standard error decreases with a larger dataset size. Table 1 presents the mean values and the standard deviations for the corresponding parameters for the analysis of 5 independent procedures of 220 Moiré patterns each. All three parameters related to the distances (R_1, R_2 and R_g) can be determined with high precision with the relative errors lower than 0.5%. While the values of A_1 and A_2 exhibit relatively higher uncertainties individually, their difference ($A_1 - A_2$) demonstrates significantly lower standard deviation. This suggests that the algorithm can effectively align the two gratings to closely matching orientations, even though the individual angles of the gratings may not be determined with equivalent accuracy. This can be understood by considering Eq. (4), which implies that

the Moiré angle is highly sensitive to discrepancies in orientations between the two gratings $(A_1 - A_2)$. The level of uncertainty, which remains below $0.1°$, for the angles of the individual gratings is acceptable for DPGI applications.

4. Discussion

The relationship between dark-field signal and correlation length can provide quantitative small-angle-scattering (SAS) information of the sample [16]. One advantage provided by DPGI is that tuning correlation length does not influence sample magnification [13]. This feature facilitates the retrieval of SAS structural information for each pixel. To accurately retrieve SAS information, the correlation length should be determined with high accuracy. Meanwhile, the contrast of the interference pattern should be maintained as high as possible, since a higher contrast will lead to a higher signal-to-noise ratio in the dark-field images [22,23]. The proposed parameter space determination process provides foundations for meeting both requirements.

Firstly, we can attain a minimum inter-grating distance of 1.5 mm in our set-up. If the inter-grating distance is measured by a ruler-based approach, the absolute error can be easily higher than 1 mm, since the exact positions of two gratings are blocked by grating holders. Consequently, more than 60% relative error is introduced when estimating the closest inter-grating distance, leading to the same relative error in estimating the minimum correlation length (see Eq. (1)). In comparison, lower than 0.5% relative errors are achievable by using the method presented in this work when determining three distances (R_1, R_2 and R_g), as illustrated in Table 1. This guarantees a much higher precision in estimating the correlation length.

A good alignment is required to guarantee high-contrast interference patterns formed in the grating interferometry [24]. To evaluate how the contrast of the patterns is influenced by the misalignment of two gratings in DPGI, with G_1 remaining at the aligned angle A_1, as given in Table 1, G_2 is rotated with a relative deviation ($\Delta\alpha_2$) from its aligned angle A_2 within the range of $-0.4°$ to $0.4°$. The inter-grating distance is maintained at 3.74 mm. At each deviated angle $\Delta\alpha_2$, the Moiré pattern is recorded and the corresponding visibility is extracted based on Eq. (9). Figure 7 plots the relationship between the deviated angle $\Delta\alpha_2$ and the averaged visibility among 2000×3000 pixels. It indicates that the highest contrast is achieved when two gratings are aligned ($\Delta\alpha_2 = 0$). Moreover, with a larger angular deviation between two gratings, the visibility reduces. If the angular deviation $|\Delta\alpha_2|$ is smaller than $0.05°$, the reduction of the visibility is lower than 0.5%, which is negligible. Since our algorithm can determine the angular deviation ($A_1 - A_2$) between two gratings with a precision better than $0.005°$, as shown in Table 1, which is one magnitude higher than $0.05°$, the highest-contrast interference patterns can be well guaranteed by the parameter space determination process.

The proposed algorithm is based on Eqs. (4) and (5), which assume that two gratings are perpendicular to the optical axis (z-axis). However, in real-world scenarios, both gratings can deviate from perfectly perpendicular positions. As shown in Fig. 8(a), though the lamellas of both gratings are aligned by the alignment process, there is an inclination angle θ between the planes of two gratings. Due to the non-uniformity of the inter-grating distance across the field of view, the generated Moiré pattern, as described by Eq. (5), will exhibit a spatially dependent distribution of periods. To evaluate the inclination angle between the planes of two gratings, one recorded Moiré pattern is analyzed when the gratings are aligned and the inter-grating distance is set at 1.954 mm, according to the results in Table 1. Firstly, this recorded Moiré pattern is divided into various sub-areas, with each one comprising 100×100 pixels. Then, the intensity oscillation of the first row within each sub-area is fitted by a cosine function, and the resulting period from the fit is regarded as the fringe period for that specific area. Therefore, a distribution of fringe periods is obtained, allowing for the calculation of a spatial distribution of the inter-grating distance according to Eq. (5). The corresponding results are shown in Fig. 8(b), in which the inter-grating distance distribution is relatively uniform along the y-axis and increases from 1.9
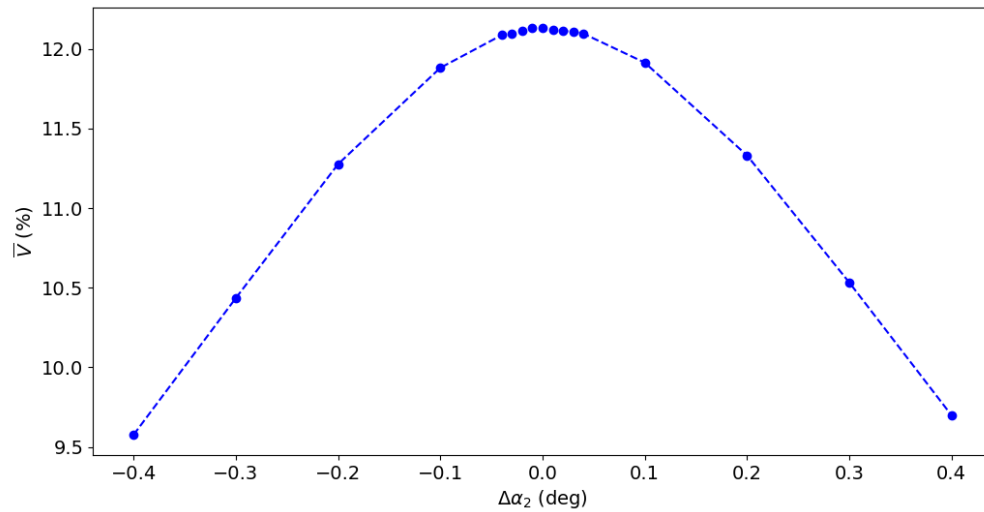
Fig. 7. Relationship between the angular deviations and averaged visibility among 2000 × 3000 pixels. With G_1 remaining at the aligned angle, G_2 is rotated with a relative deviation ($\Delta\alpha_2$) from its aligned angle within the range of $-0.4°$ to $0.4°$, with the inter-grating distance at 3.74 mm.
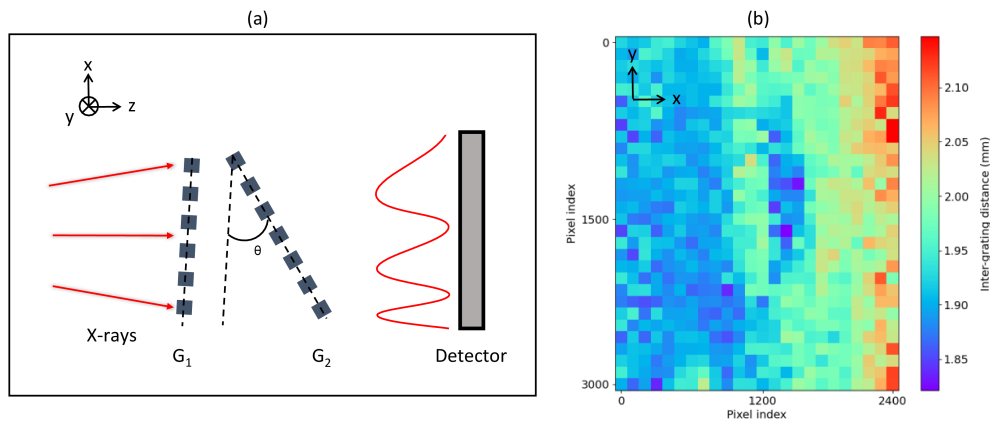

Fig. 8. (a) illustrates the situation when two gratings are not perpendicular to the z-axis after the alignment process. The inclination angle between the planes of two gratings is represented as θ. Due to the non-uniformity of the inter-grating distance across the field of view, the generated Moiré fringe exhibits a spatially dependent distribution of periods. (b) shows a spatial distribution of the inter-grating distance across the field of view, indicating an inclination angle around $0.48°$.

mm to 2.07 mm along the x-axis. This indicates an inclination angle θ between the two grating planes of approximately $0.48°$. The average inter-grating distance in Fig. 8(b) is 1.951 mm, closely matching the result determined by the parameter space determination process (1.954 mm). This indicates that the inter-grating distance determined by the parameter space determination process represents the average distance between two gratings. This is reasonable since the Fourier transform (see Fig. 3) contains all information across the full field of view. While a detailed discussion on how the inclination angle influences the parameter space determination process is beyond the scope of this work, when the inclination angle is small (eg. $0.48°$), the

algorithm demonstrates accuracy and robustness in determining geometrical parameters (see Fig. 6). Nevertheless, even with a small inclination angle, its impact should be considered when calculating the pixel-wise correlation length.

5. Conclusion

DPGI provides a promising tool in material science and medical imaging since it can provide three complementary signals from samples. Especially, its tunable correlation length offers a more straightforward approach to obtaining quantitative structural information from small-angle scattering signals. For accurate correlation length estimation and optimal grating alignment, the complete geometrical information of the set-up should be determined with high precision. To achieve this accuracy, an algorithm is developed based on the properties of Moiré patterns, to extract five geometrical parameters, including three distances and two angles. The accuracy achieved meets stringent requirements. For example, the inter-grating distance can be determined with a precision better than 10 μ, which guarantees an accurate estimation of the correlation length. Moreover, with accurate information about the angles of both gratings, the alignment of the interferometry can be automatically executed with high precision.

Appendix

As illustrated by Gabrielyan et al. [20], when two layers with periodically repeating parallel lines are superposed, the angle of the Moiré pattern is formulated as:

$$\tan \alpha_{\mathrm{m}} = \frac{T_1 \sin \alpha_2 - T_2 \sin \alpha_1}{T_1 \cos \alpha_2 - T_2 \cos \alpha_1}, \tag{10}$$

where T_1 and T_2 represent the period for each layer, while α_1 and α_2 denote the corresponding inclined angles. To avoid the infinite value yielded by the tangent function, Eq. (10) can be reformulated as:

$$\sin \alpha_{\mathrm{m}} = \frac{T_1 \sin \alpha_2 - T_2 \sin \alpha_1}{\sqrt{T_1^2 + T_2^2 - 2T_1 T_2 \cos(\alpha_2 - \alpha_1)}}, \tag{11}$$

based on trigonometry $\sin \alpha = \frac{\tan \alpha}{\sqrt{1 + \tan^2 \alpha}}$. Meanwhile, The period of the Moiré pattern is given as [20]:

$$p_{\mathrm{m}} = \frac{T_1 T_2}{\sqrt{T_1^2 + T_2^2 - 2T_1 T_2 \cos(\alpha_2 - \alpha_1)}}. \tag{12}$$

According to Eqs. (2) and (3), in DPGI the Moiré fringe for the diffraction order l is formed by two basic patterns with periods $T_1 = \frac{M_1 p_{\mathrm{g}}}{l}$ and $T_2 = \frac{M_2 p_{\mathrm{g}}}{l}$, respectively. Moreover, as the basic pattern rotates congruently with the grating, α_1 and α_2 in Eqs. (11) and (12) are equal to the rotated angles of the gratings, respectively. Therefore, the angle of the Moiré pattern formed in DPGI is deduced as:

$$\sin \alpha_{\mathrm{m}} = \frac{(R_1 + R_{\mathrm{g}}) \sin \alpha_2 - R_1 \sin \alpha_1}{\sqrt{(R_1 + R_{\mathrm{g}})^2 + R_1^2 - 2R_1(R_1 + R_{\mathrm{g}}) \cos(\alpha_2 - \alpha_1)}}, \tag{13}$$

and the period of the Moiré pattern for the diffraction order l is obtained as:

$$p_{\mathrm{m}} = \frac{(R_1 + R_2) p_{\mathrm{g}}}{l \sqrt{(R_1 + R_{\mathrm{g}})^2 + R_1^2 - 2R_1(R_1 + R_{\mathrm{g}}) \cos(\alpha_2 - \alpha_1)}}. \tag{14}$$

Disclosures. The authors declare no conflicts of interest related to this article.

Data availability. Data underlying the results presented in this paper are not publicly available at this time but may be obtained from the authors upon reasonable request. The codes along with some example data for illustrating the algorithm can be accessed via [25].

References

1. A. Momose, S. Kawamoto, I. Koyama, *et al.*, "Demonstration of x-ray talbot interferometry," Jpn. J. Appl. Phys. **42**(Part 2, No. 7B), L866–L868 (2003).
2. A. Momose, "Recent advances in x-ray phase imaging," Jpn. J. Appl. Phys. **44**(9R), 6355–6367 (2005).
3. T. Weitkamp, A. Diaz, C. David, *et al.*, "X-ray phase imaging with a grating interferometer," Opt. Express **13**(16), 6296–6304 (2005).
4. F. Pfeiffer, T. Weitkamp, O. Bunk, *et al.*, "Phase retrieval and differential phase-contrast imaging with low-brilliance x-ray sources," Nat. Phys. **2**(4), 258–261 (2006).
5. F. Pfeiffer, O. Bunk, C. Kottler, *et al.*, "Tomographic reconstruction of three-dimensional objects from hard x-ray differential phase contrast projection images," Nucl. Instrum. Methods Phys. Res., Sect. A **580**(2), 925–928 (2007).
6. F. Pfeiffer, M. Bech, O. Bunk, *et al.*, "Hard-x-ray dark-field imaging using a grating interferometer," Nat. Mater. **7**(2), 134–137 (2008).
7. T. Donath, F. Pfeiffer, O. Bunk, *et al.*, "Toward clinical x-ray phase-contrast ct: demonstration of enhanced soft-tissue contrast in human specimen," Invest. Radiol. **45**(7), 445–452 (2010).
8. M. Engelhardt, J. Baumann, M. Schuster, *et al.*, "High-resolution differential phase contrast imaging using a magnifying projection geometry with a microfocus x-ray source," Appl. Phys. Lett. **90**(22), 224101 (2007).
9. P. Zhu, K. Zhang, Z. Wang, *et al.*, "Low-dose, simple, and fast grating-based x-ray phase-contrast imaging," Proc. Natl. Acad. Sci. **107**(31), 13576–13581 (2010).
10. M. Stampanoni, Z. Wang, T. Thüring, *et al.*, "Toward clinical differential phase contrast mammography: preliminary evaluations and image processing schemes," J. Instrum. **8**(05), C05009 (2013).
11. H. F. Talbot, "Lxxvi. facts relating to optical science. no. iv," The London, Edinburgh, Dublin Philos. Mag. J. Sci. **9**(56), 401–407 (1836).
12. H. Miao, A. Panna, A. A. Gomella, *et al.*, "A universal moiré effect and application in x-ray phase-contrast imaging," Nat. Phys. **12**(9), 830–834 (2016).
13. M. Kagias, Z. Wang, K. Jefimovs, *et al.*, "Dual phase grating interferometer for tunable dark-field sensitivity," Appl. Phys. Lett. **110**(1), 014105 (2017).
14. F. Pfeiffer, O. Bunk, C. Schulze-Briese, *et al.*, "Shearing interferometer for quantifying the coherence of hard x-ray beams," Phys. Rev. Lett. **94**(16), 164801 (2005).
15. A. Yan, X. Wu, and H. Liu, "Sample phase gradient and fringe phase shift in dual phase grating x-ray interferometry," Opt. Express **27**(24), 35437–35447 (2019).
16. M. Strobl, "General solution for quantitative dark-field contrast imaging with grating interferometers," Sci. Rep. **4**(1), 7243 (2014).
17. F. Prade, A. Yaroshenko, J. Herzen, *et al.*, "Short-range order in mesoscale systems probed by x-ray grating interferometry," Europhys. Lett. **112**(6), 68002 (2015).
18. A. Yan, X. Wu, and H. Liu, "Quantitative theory of x-ray interferometers based on dual phase grating: fringe period and visibility," Opt. Express **26**(18), 23142–23155 (2018).
19. A. Yan, X. Wu, and H. Liu, "Predicting fringe visibility in dual-phase grating interferometry with polychromatic x-ray sources," J. X-Ray Sci. Technol. **28**(6), 1055–1067 (2020).
20. E. Gabrielyan, "The basics of line moiré patterns and optical speedup," arXiv, arXiv:physics/0703098 (2007).
21. C. Organista, M. Kagias, R. Tang, *et al.*, "Optimization of the visibility of a tunable dual-phase x-ray grating interferometer," Opt. Continuum **2**(1), 232–248 (2023).
22. M. Chabior, T. Donath, C. David, *et al.*, "Signal-to-noise ratio in x ray dark-field imaging using a grating interferometer," J. Appl. Phys. **110**(5), 053105 (2011).
23. S. Spindler, D. Etter, M. Rawlik, *et al.*, "The choice of an autocorrelation length in dark-field lung imaging," Sci. Rep. **13**(1), 2731 (2023).
24. K. Deng, J. Li, and W. Xie, "Modeling the moire fringe visibility of talbot-lau x-ray grating interferometry for single-frame multi-contrast imaging," Opt. Express **28**(18), 27107–27122 (2020).
25. R. Tang, "Geometrical space determination, GitHub (2020) https://github.com/rtangpy/Grating-alignment.